Imprint of f(R) gravity on nonlinear structure formation

(Article begins on next page)

03 May 2024

The Imprint of f(R) Gravity on Non-Linear Structure Formation

Ixandra Achitouv[1,2*], Marco Baldi[3,4,5], Ewald Puchwein[6], and Jochen Weller[7,8,9]

[1] Centre for Astrophysics & Supercomputing, Swinburne University
of Technology, P.O. Box 218, Hawthorn, VIC 3122, Australia

[2] ARC Centre of Excellence for All-sky Astrophysics (CAASTRO), 44 Rosehill St, Redfern, NSW 2016, Australia

[3] Dipartimento di Fisica e Astronomia, Alma Mater Studiorum
Università di Bologna, viale Berti Pichat, 6/2, I-40127 Bologna, Italy

[4] INAF - Osservatorio Astronomico di Bologna, via Ranzani 1, I-40127 Bologna, Italy

[5] INFN - Sezione di Bologna, viale Berti Pichat 6/2, I-40127 Bologna, Italy

[6] Kavli Institute for Cosmology Cambridge and Institute of Astronomy,
University of Cambridge, Madingley Road, Cambridge CB3 0HA, UK

[7] Universitäts-Sternwarte, Fakultät für Physik, Ludwig-Maximilians
Universität München, Scheinerstr. 1, 81679 München, Germany

[8] Excellence Cluster Universe, Boltzmannstr. 2, 85748 Garching, Germany

[9] Max Planck Institute for Extraterrestrial Physics, Giessenbachstr. 1, 85748 Garching, Germany

We test the imprint of $f(R)$ modified gravity on the halo mass function, using N-body simulations and a theoretical model developed in [44]. We find a good agreement between theory and simulations $\sim 5\%$. We extend the theoretical model to the conditional mass function and apply it to the prediction of the linear halo bias in $f(R)$ gravity. Using the halo model we obtain a prediction for the non-linear matter power spectrum accurate to $\sim 10\%$ at $z = 0$ and up to $k = 2\text{h/Mpc}$. We also study halo profiles for the $f(R)$ models and find a deviation from the standard general relativity result up to 40%, depending on the halo masses and redshift. This has not been pointed out in previous analysis. Finally we study the number density and profiles of voids identified in these $f(R)$ N-body simulations. We underline the effect of the bias and the sampling to identify voids. We find significant deviation from GR when measuring the $f(R)$ void profiles with $f_{R0} < -10^{-6}$.

I. INTRODUCTION

As cosmology is approaching the epoch of precision measurements with a number of current and upcoming observational enterprises – as e.g. BOSS [1], HETDEX [2], DES [4], DESI [5], eBOSS [6], WFIRST [7], LSST [3] and EUCLID [9] – aiming to constrain the basic cosmological parameters to percent precision, significant efforts are required to improve theoretical and numerical modeling of possible deviations from the standard ΛCDM scenario. In particular, some of the most ambitious observational enterprises of the next decade (such as e.g. DES and Euclid) will focus on testing and constraining possible alternatives to the cosmological constant Λ as the source of the observed accelerated expansion of the Universe [10, 11]. In fact, despite the cosmological constant remaining so far the simplest possible explanation of the cosmic acceleration that consistently accounts for available observations [see e.g. 6, 12, 13], its theoretical footings represent an open problem for both cosmology and theoretical particle physics as the observed energy scale associated with Λ appears to be unnaturally small (e.g. [15]).

A possible extension to the cosmological constant paradigm are represented by a dynamical Dark Energy field whose background density evolves in time along the cosmic history [see e.g. 14, 16] – possibly also featuring

direct interactions with other matter fields [17–20, 25]. Another possibility are modifications of General Relativity (GR) on large scales [as e.g. in 29–31, 40, 41, 43], resulting in a modification of the gravitational instability processes that leads to the formation of cosmic structures. The simplest and most widely investigated modification of the gravitational theory with a relevant impact on cosmology is the class of scalar-tensor theories known as $f(R)$ gravity, where the standard Einstein-Hilbert Action is modified by adding to the Ricci scalar R a further term given by an arbitrary function $f(R)$:

$$S = \int \mathrm{d}^4x \, \sqrt{-g} \left(\frac{R + f(R)}{16\pi G} + \mathcal{L}_m \right), \qquad (1)$$

where G is Newton's gravitational constant, g is the determinant of the metric tensor $g_{\mu\nu}$, and $\mathcal{L}_m$ is the Lagrangian of matter content of the Universe. By suitably choosing the form of the function $f(R)$ it is possible to tune the model so to have an expansion history arbitrarily close to the standard Λ cold dark matter (CDM) scenario [30], thereby matching present background observations and confining possible deviations from the standard model only in the evolution of density perturbations in both the linear and nonlinear regimes [35–37, 42, 48].

Consistency with solar system tests of scalar-tensor theories [38, 39] additionally requires that standard General Relativity is recovered in our local environment, which can be ensured in $f(R)$ theories by the so-called *Chameleon* screening mechanism [21] that suppresses the deviation from standard gravity in high-density environments such as the Milky Way.

———

[*] E-mail:iachitouv@swin.edu.au

In such Chameleon $f(R)$ models the point at which screening is triggered is controlled by the background field amplitude f_{R0} (see Sec. II). Smaller values of $|f_{R0}|$ correspond to more aggressive screening and hence smaller deviations from GR. Observational constraints on $|f_{R0}|$ have been obtained from a multitude of different object types and scales. An overview of the various constraints is given, e.g., in [45]. Observations on large scales and in galaxy cluster can typically rule out models with $|f_{R0}| \gtrsim 10^{-4}$ [e.g. 46]. Solar system test roughly require $|f_{R0}| \lesssim 10^{-6}$ [30]. Even stronger constraints $|f_{R0}| \lesssim 5 \times 10^{-7}$ have been obtained in a quite different regime from distance indicators such as Cepheid variables in potentially unscreened dwarf galaxies [47]. Some of the models that we will consider here, like $|f_{R0}| = 10^{-4}$, are hence already in quite significant tension with the data. We will nevertheless include them to test whether our findings are robust even for larger deviations from GR.

In this work, we use the N-body simulations described in [48] to look at the imprint of $f(R)$ models on the abundance of halos. We compare the results of the N-body simulations to the results of the spherical collapse model developed in [44]. We extend this theoretical investigation to the conditional mass function with a drifting diffusive barrier and a mean value, which depends on the halo masses according to the $f(R)$ models we consider. We deduce the linear halo bias for $f(R)$ gravity, which allows us to test the prediction of the non-linear matter power spectrum using the halo model [84]. We also compare the halo profiles we measure in the simulations to the GR case. Finally, we study the imprint of $f(R)$ models on the void profiles and void abundances. These are particularly interesting for considering deviations from GR. We measure void profiles in two cases: firstly, we identify the voids in each simulation and stack their profiles. Secondly, we identify the voids in the GR simulation which have the same initial conditions as the $f(R)$ simulations and measure the profiles in the $f(R)$ simulation by using the GR positions of the voids.

The outline of this paper is as follows: In section II we describe the modified gravity model assumed here, in section III we present the N-body simulation results for the mass function in $f(R)$ and compare them to the model presented in [44]. In section IV we predict the linear halo bias for $f(R)$ models. In section V we study the halo profiles in $f(R)$ simulations and the deviation compared to the GR results. In section VI we use the halo model to predict the non-linear power spectrum in the $f(R)$ and compare to the GR results. In Sec.VII we measure the abundance of voids, while in section VIII we study the profile of voids in the $f(R)$ simulations. Finally, in section IX we draw our conclusions.

II. THE MODIFIED GRAVITY MODEL

In this work we will focus on the Chameleon $f(R)$ modified gravity model introduced in [30], in which the function $f(R)$ in Eq. (1) is assumed to be

$$f(R) = -m^2 \frac{c_1 \left(\frac{R}{m^2}\right)^n}{c_2 \left(\frac{R}{m^2}\right)^n + 1},$$ (2)

where $m^2 \equiv H_0^2 \Omega_m$. H_0 and Ω_m are the Hubble and matter density parameter at $z = 0$. n, c_1 and c_2 are free parameters. For a viable choice, we want models with a background expansion history close to ΛCDM so that cosmological constraints are not violated. This can be achieved if we require $c_2(R/m^2)^n \gg 1$. $f(R)$ can then be expanded as $f(R) = -m^2 c_1/c_2 + O((m^2/R)^n)$. The ΛCDM background behaviour is recovered by setting the zeroth order term $-m^2 c_1/c_2$ equal to the term that would appear in Eq. (1) in ΛCDM, i.e. to -2Λ, where Λ is the desired value of the cosmological constant. This results in a relation between the parameters c_1 and c_2,

$$\frac{c_1}{c_2} = 6 \frac{\Omega_\Lambda}{\Omega_m},$$ (3)

where Ω_Λ is the desired vacuum energy density in units of the critical density of the Universe. In the following we will consider only the case $n = 1$, so that there is only one degree of freedom left in the choice of the model parameters.

In such models, $f_R \equiv \frac{df(R)}{dR}$ can be interpreted as a scalar degree of freedom that governs the dynamics of the model. Viable models require $|f_R| \ll 1$. In this case and in the quasistatic approximation, which is justified for sub-horizon perturbations [34, 49], a field equation for f_R can be obtained from Eq. (1) [see, e.g., 30],

$$\nabla^2 f_R = \frac{1}{3c^2} \left(\delta R - 8\pi G \delta\rho\right),$$ (4)

where c is the speed of light and $\delta\rho$ and δR are the density and scalar curvature perturbations respectively. Note that this equation is non-linear as δR depends on f_R. In particular in the limit chosen above, i.e. $c_2(R/m^2)^n \gg 1$, we find

$$f_R \approx -n \frac{c_1}{c_2^2} \left(\frac{m^2}{R}\right)^{n+1},$$ (5)

which for $n = 1$ translates to $f_R \propto R^{-2}$. Using the background field amplitude at $z = 0$, f_{R0}, as a parameter to fix the remaining degree of freedom in the model choice and define the model completely, we obtain

$$\delta R = R_0 \left(\sqrt{\frac{f_{R0}}{f_R}} - 1\right).$$ (6)

Together with Eq. (4) this yields the main non-linear partial differential equations that needs to be solved in this model. Further details about the numerical solution of this equation in the cosmological simulations are given

in [48]. Once a solution for f_R and hence δR has been found, the gravitational potential ϕ can be obtained from [see, e.g., 30, 50]

$$\nabla^2 \phi = \frac{16\pi G}{3}\delta\rho - \frac{1}{6}\delta R, \qquad (7)$$

which for given δR is a linear Poisson equation. All the non-linearities of the model are encoded in the modified source term, which of course differs from Newtonian gravity. Gravitational accelerations can then be computed from the potential in the usual way.
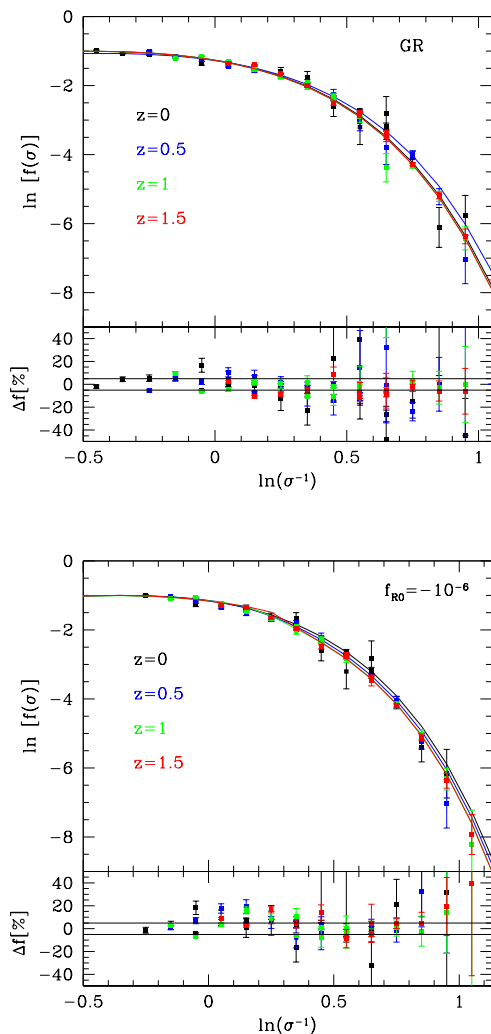
III. MASS FUNCTION

FIG. 1: Multiplicity function for GR (ΛCDM) and $f_{R0} = 1 - 0^{-6}$ at various redshifts. Solid lines are theory, squares are from simulations. Lower panels show the relative difference. Black solid lines show $\pm 5\%$ differences.
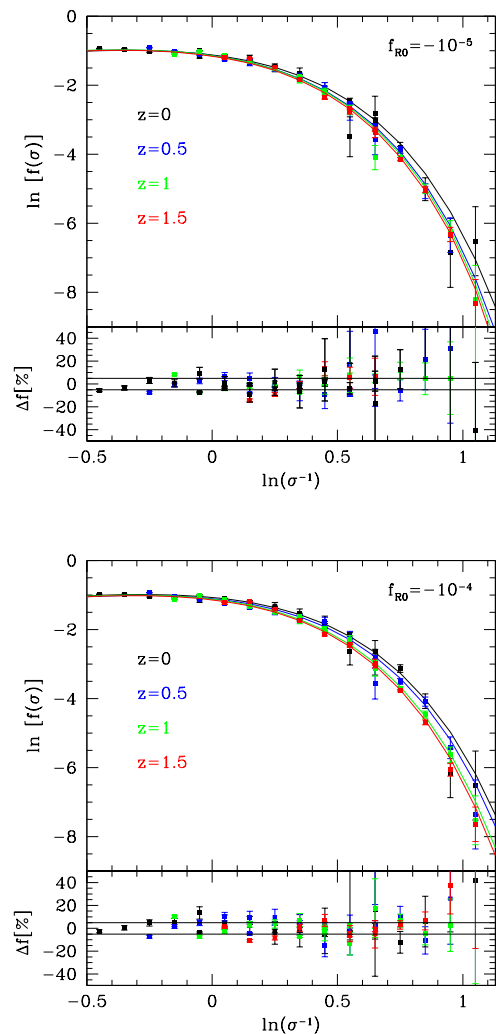

FIG. 2: Multiplicity function for $f_{R0} = -10^{-5}$ and $f_{R0} = -10^{-4}$ at various redshifts. Solid lines are theory, squares are from simulations. Lower panels show the relative difference. Black solid lines show $\pm 5\%$ differences.

In recent years the abundance of galaxy clusters as a cosmological probe has been firmly established [60][22][13][24][23]. In [44], the authors have solved the spherical collapse threshold for a class of $f(R)$ modified gravity models. The linear solution extrapolated to several redshifts was used to predict the halo mass function. In this section we compare the theoretical mass function of [44] to the N-body simulations of [48].

In the excursion set approach [51] based upon [52], the halo mass function can be expressed as

$$\frac{dn}{dM} = f(\sigma)\frac{\rho_m}{M^2}\frac{d\log\sigma^{-1}}{d\log M}, \qquad (8)$$

where $f(\sigma) = 2S\mathcal{F}(S)$ is the multiplicity function, $\mathcal{F}(S)$

is the so called first-crossing distribution predicted by the excursion set theory and ρ_m is the comoving mean matter density field. The variance σ and the variance squared S are defined as

$$S \equiv \sigma^2(z, R(M)) = \frac{1}{2\pi^2} \int \mathrm{dk}\, \mathrm{k}^2\, \mathrm{P(k,z)} |\tilde{\mathrm{W}}|^2(\mathrm{k}, \mathrm{R(M)}) \tag{9}$$

where $\tilde{W}(k, R)$ is the Fourier transform of a filter function and $P(k, z)$ the redshift dependent linear matter power spectrum.

The derivative of the variance with respect to the mass is in principle sensitive to the linear background evolution and thus to the cosmological model. However, we follow [44] in using the linearly evolved ΛCDM power spectrum in Eq. (9) even in the case of $f(R)$ and encoding all modified gravity deviations in a redshift and mass dependent collapse threshold instead.

The multiplicity function encapsulates all the non-linear collapse of halos and is therefore the fundamental ingredient that we want to predict. The basic idea of [51, 52] is to predict the formation of a halo when the linear overdensity δ smoothed on a scale R(M) is above a critical threshold B. To avoid assigning more than one mass to the halo, the scale R is chosen to be the largest one for which δ crosses the threshold B. The halo mass is therefore defined by the volume enclosed by the filter function at the scale R which satisfies $\delta(R) = B$, times the mean matter density field. Assuming a random position (e.g. $\vec{x} = 0$), the smoothed overdensity $\delta(R)$ is given by

$$\delta(R) = \frac{1}{(2\pi)^3} \int \mathrm{d}^3 \mathrm{k} \tilde{\mathrm{W}}(\mathrm{k}, \mathrm{R}) \tilde{\delta}(\mathrm{k}). \tag{10}$$

For Gaussian initial conditions a top-hat filter in Fourier space and and GR spherical collapse, one can compute exactly the probability density function of $\delta(R) < \delta_c$: $\Pi(\delta, S)$ [51]. Thus, the fraction of volume collapsed into objects on scale R or larger becomes :

$$F(R) = 1 - \int_{-\infty}^{B} \Pi(\delta, S(R)), \tag{11}$$

from which the first-crossing rate is given by $\mathcal{F}(S) = dF(R)/dS(R)$. In [53] the authors used a path integral technique to compute $\Pi(\delta, S)$ assuming a top-hat filter in real space. This filter is convenient since it defines spherical volumes unlike a top-hat filter in Fourier space (sk-filter). In [54], the solution of the first-crossing rate for overdensity smoothed with a top-hat filter in real space (sx-filter) has been extended to the case of a stochastic threshold B. In this case, the barrier is no longer deterministic and is defined by a Gaussian distribution with a mean value $\bar{B} = \delta_c$ and a variance $< B(S_1)B(S_2) >= D_B \min(S_1, S_2)$. The

same model was extended [55–57] to the case where $\bar{B} = \delta_c + \beta S$. For a positive β, this barrier increases with the variance. This implies that low mass halos require a larger linear overdensity to collapse in agreement with [67]. The analytical prediction for this model of barrier and filter (ie: top-hat in real space) was tested against the exact numerical solution [56, 61] by performing Monte Carlo random walks [51]. It was shown that the analytical solution reproduces the exact solution within 5%. Furthermore, this barrier model predicts a halo mass function in excellent agreement with N-body simulations [55] and is consistent with the initial conditions [61, 62] (ie: the parameters of the barrier can be measured in the initial conditions of the N-body simulation). The choice of the linear drifting term βS over more generic functions (e.g. βS^γ) was motivated by the fact that the analytical solution for the multiplicity function is exact for the sk-filter. While this model is sufficient for predicting very accurate mass functions in the ΛCDM case, it needs to be extended if one considers barriers with a mean value which does not scale linearly.

In [44], the author has computed the spherical collapse threshold δ_c in the case of an $f(R)$ model. In order to obtain such threshold, they evolved a top hat profile of different initial perturbations using the full modified Einstein and fluid equations in simulation (section III A in [44]). Then they provide an interpolation function which fit their solution for different redshift and $f(R)$ parameters. In this model, the threshold is deterministic but unlike GR, the spherical threshold now depends on the mass of the halo. The numerical fit of [44] is given by:

$$\delta_c(z, M, f_{R0}) = \delta_c^\Lambda(z) \left\{ 1 + b_2 (1+z)^{-a_3} \times \right.$$
$$\left. \left(m_b - \sqrt{m_b^2 + 1} \right) + b_3 (\tanh m_b - 1) \right\}, \tag{12}$$

$$m_b(z, M, f_{R0}) = (1+z)^{a_3} \times \tag{13}$$
$$\left(\log_{10}[M/(M_\odot h^{-1})] - m_1(1+z)^{-a_4} \right),$$
$$m_1(f_{R0}) = 1.99 \log_{10} |f_{R0}| + 26.21,$$
$$b_2 = 0.0166,$$
$$b_3(f_{R0}) = 0.0027 \cdot (2.41 - \log_{10} |f_{R0}|),$$
$$a_3(f_{R0}) = 1 + 0.99 \exp\left[-2.08(\log_{10}|f_{R0}| + 5.57)^2 \right],$$
$$a_4(f_{R0}) = (\tanh\left[0.69 \cdot (\log_{10}|f_{R0}| + 6.65) \right] + 1) 0.11,$$

where z is the redshift, M the mass and $f_{R0} = \frac{df}{dR}(R_0)$ with R_0 modified gravity curvature parameter today [30]. Using Eq.(12) for the spherical collapse, and keeping the drifting term β, the multiplicity function for the sx-filter (id: top-hat in real space), is given by [44]:

$$f(\sigma) = f_{\mathrm{sx}}^{\mathrm{GR}}(\sigma) \frac{f_{\mathrm{sk}}(\sigma)}{f_{\mathrm{sk}}^{\mathrm{GR}}(\sigma)} + \mathcal{O}(\kappa^2) \qquad (14)$$

where κ is called the non-Markovian amplitude parameter, $\kappa \sim 0.46$. The non-Markovian corrections arise from the sx-filter (e.g. [53][62]). This last equation assumes that the non-Markovian corrections are approximately universal. The different contributions are

$$f_{\mathrm{sx}}^{\mathrm{GR}}(\sigma) \simeq f_{\mathrm{sk}}^{\mathrm{GR}}(\sigma) + f_{1,\beta=0}^{m-m}(\sigma) + f_{1,\beta^{(1)}}^{m-m}(\sigma) + f_{1,\beta^{(2)}}^{m-m}(\sigma), \qquad (15)$$

with

$$f_{\mathrm{sk}}^{\mathrm{GR}}(\sigma) = \frac{\delta_c}{\sigma} \sqrt{\frac{2a}{\pi}} \, e^{-\frac{a}{2\sigma^2}(\delta_c + \beta\sigma^2)^2}, \qquad (16)$$

$$f_{1,\beta=0}^{m-m}(\sigma) = -\tilde{\kappa} \frac{\delta_c}{\sigma} \sqrt{\frac{2a}{\pi}} \left[e^{-\frac{a\delta_c^2}{2\sigma^2}} - \frac{1}{2} \Gamma\left(0, \frac{a\delta_c^2}{2\sigma^2}\right) \right], \quad (17)$$

$$f_{1,\beta^{(1)}}^{m-m}(\sigma) = -a\,\delta_c\,\beta \left[\tilde{\kappa}\,\mathrm{Erfc}\left(\delta_c\sqrt{\frac{a}{2\sigma^2}}\right) + f_{1,\beta=0}^{m-m}(\sigma) \right], \qquad (18)$$

$$f_{1,\beta^{(2)}}^{m-m}(\sigma) = -a\,\beta \left[\frac{\beta}{2}\sigma^2 f_{1,\beta=0}^{m-m}(\sigma) + \delta_c\, f_{1,\beta^{(1)}}^{m-m}(\sigma) \right]. \quad (19)$$

with $a = 1/(1 + D_B)$. These terms are computed using a path integral technique (e.g. [53] [56]) and converge quickly for realistic values of the barrier parameters [61]. Finally, $f_{sk}(\sigma)$ is the prediction of the multiplicity function for a barrier with generic mean values and a Gaussian distribution. For Eq.(12) we have [44]:

$$f_{sk}(\sigma) \simeq \sqrt{\frac{2a}{\pi}} e^{-a\bar{B}^2/(2\sigma^2)} \frac{1}{\sigma} \left(\bar{B} - \sigma^2 \frac{d\bar{B}}{d\sigma^2} \right) \qquad (20)$$

with $\bar{B} = \delta_c(M, f_{R0}) + \beta S$. Since the spherical collapse for GR is very different from the one in a $f(R)$ model, we should assume that β and D_B are not necessarily the same for GR and $f(R)$ models. In both cases there is no theory available to predict these parameters. In [61, 62] these parameters were measured in the initial conditions. In this work we adopt the approach of [55, 56] to determine β and D_B. We compute the best fitting values of β and D_B which reproduce the multiplicity function of the N-body simulations. We start by comparing $f_{sx}^{GR}(\sigma)$ to the N-body simulation of [48] where halos are identified using a Friend-of-Friend (FoF) algorithm with linking length $b = 0.2$. In order to simplify the analysis, we assume that for the ΛCDM case, the multiplicity function is universal. Thus for all redshifts we find that the best fitting values are $\beta = 0.05$ and $D_B = 0.34$. Then we recompute a best fit for β and D_B in Eq.(20), which are

	$f_{R0} = -10^{-4}$	$f_{R0} = -10^{-5}$	$f_{R0} = -10^{-6}$
	β, D_B	β, D_B	β, D_B
$z = 0.0$	0.05 , 0.3	0.06 , 0.3	0.08 , 0.42
$z = 0.5$	0.08 , 0.29	0.06 , 0.26	0.08 , 0.42
$z = 1.0$	0.08 , 0.22	0.06 , 0.25	0.09 , 0.4
$z = 1.5$	0.1 , 0.2	0.09 , 0.23	0.09 , 0.4

TABLE I: values of β, D_B in Eq.(20) for different redshifts and f_{R0} parameters. For the GR multiplicity function Eqns.(15,16) we neglect the non-universal behaviour of the multiplicity function: for all redshifts we set $\beta = 0.05$ and $D_B = 0.34$

specific to the modified gravity model. These values are reported in Table I.

Note that on average β tends to increases with redshift while D_B tends to decrease with redshift in agreement with [62]. This means that the threshold becomes more deterministic at high redshift. However, the underline physics of the β, D_B parameters can be observe only with high resolution simulations that can cover with accuracy a broad mass range (see [62]). Using Eq.(14) with the values of Tab I we obtain the prediction shown in Figs. 1-2. The multiplicity functions measured in the N-body simulations are represented by the squares and Eq.(14) by the solid lines. Lower panels show the relative difference between theory and N-body simulations. The black lines mark the $\pm 5\%$ deviation. As we can see, for the various f_{R0} parameters and at different redshifts, our prediction remains very accurate over all ranges of mass.

The deviation of the halo mass function between ΛCDM and the $f(R)$ model is discussed in [48]. In Figs. 3-4 we show the ratio between the $f(R)$ and the ΛCDM multiplicity functions. The solid lines are the theoretical ratio using the multiplicity functions of Fig. 1 while the squares are the ratio from the N-body simulations. Different colours correspond to different redshifts according to the legend. Typically the difference between GR and f(R)increases with mass. For $f_{R0} = -10^{-4}$ and over the mass ranges probed by the N-body simulations, the difference reaches $\sim 50\%$. For $f_{R0} = -10^{-5}, -10^{-6}$ the difference is $\sim 30\%, 20\%$ respectively. The bumps present for the $f_{R0} = -10^{-6}$ are specific to the trend of the spherical collapse model given by Eq.(12). Similar trends are shown in [68].

IV. CONDITIONAL MASS FUNCTION AND LINEAR HALO BIAS FOR MODIFIED GRAVITY

The linear halo bias measures how halos are biased compared to the underlying dark matter density field on large scales. It can be measured by taking the square root of the ratio between the 2-point correlation function of halos and the one of the underlying matter density field. The peak-background split approach [63–66] provides a theoretical framework to compute it. The idea is to measure the abundance of halos formed at an ini-
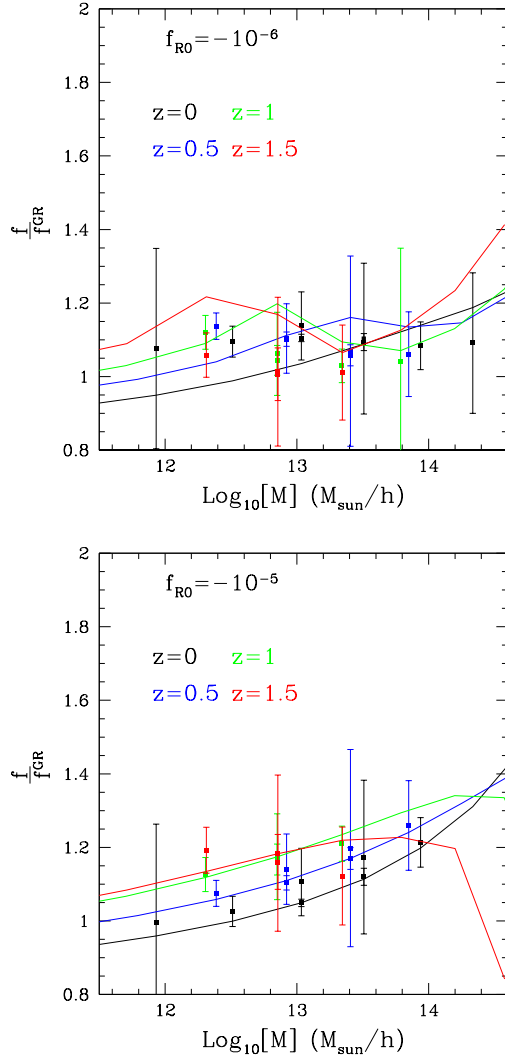
FIG. 4: Modified gravity multiplicity function with respect to ΛCDM multiplicity function for $f_{R0} = -10^{-4}$. The solid lines show the theory while the squares show the N-body simulation result.

FIG. 3: Modified gravity multiplicity function for $f_{R0} = -10^{-6}$ and $f_{R0} = -10^{-5}$ with respect to ΛCDM multiplicity function. The solid lines show the theory while the squares show the N-body simulation result.

FIG. 5: $f(\sigma)$ from Eqn.(32) is plotted as a solid line and the exact Monte Carlo solution is shown by squares for different conditions (δ_m, S_m) (red and blue). The upper panel correspond to a barrier with parameters $(\delta_c = 1.673, \beta = 0.1, \gamma = 0.5)$ while the lower panel is for $(\delta_c = 1.673, \beta = 0.1, \gamma = 1.5)$.

tial overdensity $\delta_0(r_0)$ relative to the unconditional mass function. Assuming $r_0 \to \infty$ (e.g. $\delta_0 \ll 1$) then the linear halo bias is given by

$$b_h = 1 + \frac{1}{\mathcal{F}(S|\delta_0 = 0, r_0 = 0)} \frac{\partial \mathcal{F}(S|\delta_0, r_0 = 0)}{\partial \delta_0}\Big|_{\delta_0 = 0} \tag{21}$$

In this section we compute the conditional mass function for a diffusing barrier with generic drift. We first consider the general case without taking any limit for the perturbations δ_0. Then we derive the linear bias and test the robustness of our prediction using Monte Carlo random walks[51].

In [53], the authors have developed a path-integral framework where the excursion set approach can be re-
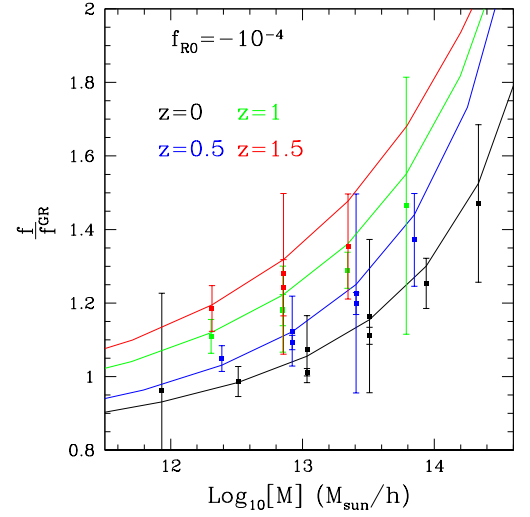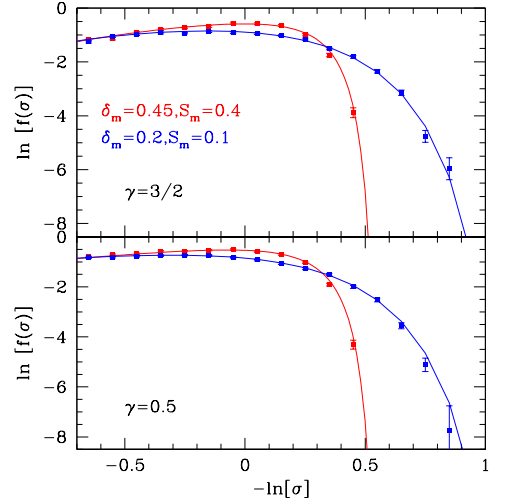
formulated for generic filters. By discretizing the variable S in step ΔS such that $S_k = k\Delta S$ with $k = 1, .., n$, the probability density (PDF) of finding an overdensity δ on a scale $S(R)$, without crossing the threshold B on a scale $S' < S$ is given by

$$\Pi(\delta_0, \delta_n, S_n) = \int_{-\infty}^{B} d\delta_1 ... \int_{-\infty}^{B} d\delta_{n-1} W(\delta_0, ..\delta_n, S_n) \tag{22}$$

where

$$W(\delta_0,...\delta_n, S_n) = \int \mathcal{D}\lambda e^{i\sum_{i=1}^n \lambda_i \delta_i} \langle e^{-i\sum_{i=1}^n \lambda_i \delta(S_i)} \rangle. \quad (23)$$

The measure $\mathcal{D}\lambda \equiv d\lambda_1/(2\pi)...d\lambda_n/(2\pi)$ and the brackets $\langle...\rangle$ refer to an ensemble average of the random walks. This is the well-known exp function of the partition function used in particle physics. The fraction of collapsed halos is also derived using Eq.(11) once the PDF is known. In [69] the probability to get δ_n on scale S_n knowing that the smoothed field had a value δ_m on scale S_m is

$$P(\delta_n, S_n|\delta_m, S_m) = \frac{\int_{-\infty}^B d\delta_1...d\hat{\delta}_m... \int_{-\infty}^B d\delta_{n-1} W(\delta_0,...,\delta_m,...\delta_n, S_n)}{\int_{-\infty}^B d\delta_1... \int_{-\infty}^B d\delta_{m-1} W(\delta_0...\delta_m, S_m)} \quad (24)$$

where $d\hat{\delta}_m$ means we do not integrate over δ_m. Therefore the first-crossing distribution is

$$\mathcal{F}(S|\delta_m, S_m) = -\int_{-\infty}^B \frac{\partial P(\delta_n, S_n|\delta_m, S_m)}{\partial S_n}. \quad (25)$$

For a sharp-k filter (sk) Eq.(24) is greatly simplified [56, 69]. The Markovian property implies that

$$P(\delta_n, S_n|\delta_m, S_m) = \int_{-\infty}^B d\delta_{m+1}... \int_{-\infty}^B W(\delta_m...\delta_n, S_n - S_m) \quad (26)$$

The random walk analogy for this equation implies the system does not memorize previous steps, such that the probability to pass by $\delta_m(S_m)$ is the same as starting the random walk on scale S_m with initial values δ_m instead of $(\delta_0 = 0, S_0 = 0)$. This leads to the rescaling $\delta_0 \to \delta_m$, $S \to S - S_m$ in the multiplicity function. This is exact for constant threshold B, as in the GR spherical collapse case. In the case of a diffusing barrier with a sk filter, we should carefully rewrite the previous equations. In the model of [56, 61] the barrier is not correlated with the smoothed field ($< B(S)\delta(S') >= 0$). The barrier PDF is defined by

$$\Pi_B(B_0, B_n, S_n) = \frac{1}{\sqrt{2\pi D_B S}} e^{-\frac{(B-\bar{B})^2}{2D_B S}}. \quad (27)$$

We assume first $\bar{B} = B_0$, a constant, such that the barrier PDF satisfies the Fokker-Planck Equation $\partial \Pi_B/\partial S = \frac{D_B}{2}\partial^2 \Pi_B/\partial B_n^2$. The first-crossing distribution then becomes

$$\mathcal{F}(S|\delta_m, S_m) = -\frac{\partial}{\partial S} \int_{-\infty}^\infty dB \, \Pi_B(B_0, B_n, S) \int_{-\infty}^B d\delta \, \Pi(\delta_m, \delta_n, S_m - S_n). \quad (28)$$

The PDF $\Pi(\delta_m, \delta_n, S_m - S_n)$ is a solution of the Fokker-Planck Equation: $\partial\Pi/\partial S = \frac{1}{2}\partial^2\Pi/\partial\delta_n^2$. Furthermore the solution must satisfy the absorbing boundary condition $\Pi(\delta_m, \delta_n = B, S_m - S_n) = 0$ and the initial condition that $\Pi(\delta_m, \delta_n, S_m - S_n = 0) = \delta_D(\delta_n - \delta_m)$, leading to the solution [51]

$$\Pi(\delta_m, \delta_n, S_n - S_m) = \frac{1}{\sqrt{2\pi(S_n - S_m)}}\{e^{-\frac{(\delta_n-\delta_m)^2}{2(S_n-S_m)}} - e^{-\frac{(2B-\delta_n-\delta_m)^2}{2(S_n-S_m)}}\}. \quad (29)$$

Plugging Eq.(29) into Eq.(28) leads to

$$\mathcal{F}(S|\delta_m, S_m) = -\frac{\partial}{\partial S} \int_{-\infty}^\infty dB \, \Pi_B(B_0, B_n, S) \, \text{Erf}\left[\frac{B - \delta_m}{\sqrt{2(S - S_m)}}\right] \quad (30)$$

The derivative with respect to S leads to two terms: the derivative of the error function term and the derivative of the term in Eq.(27). Using of the Fokker-Planck equation and Eq.(27) we perform an integration by parts leading to

$$\mathcal{F}(S|\delta_m, S_m) = \sqrt{\frac{1}{2\pi}} \frac{(B_0 - \delta_m)(1 + D_B)}{[(1 + D_B)S - S_m]^{3/2}} e^{-\frac{(B_0-\delta_m)^2}{2(1+D_B)S-2S_m}}. \quad (31)$$

From this expression we can see that setting $D_B = 0$ leads to the original solution of [51]. This solution for $\delta_m = 0$ is also in agreement with [69] who use for the barrier in Eqn.(27) with $\bar{B} = \delta_c$. For modified gravity we want to extend Eq.(31) to any generic mean value $\bar{B}$ so that we can use Eq.(12), which is no longer a constant but a function of the mass $M(S)$. For a generic barrier, the first-crossing does not have an exact analytical solution for the unconditional and conditional mass function. This is due to the absorbing boundary condition, which can not be fulfilled except for a constant or a linear barrier. In [44], the authors computed an approximation for the unconditional multiplicity function with a generic barrier . In [44], for the functional trend of Eq.(12), the authors found that Eq.(20) reproduces the exact Monte-Carlo solution within 5%. In what follows we propose to extend this approximation to the conditional mass function by taking

$$f(S|\delta_m, S_m) \simeq \sqrt{\frac{2}{\pi}}\left[\bar{B}(S) - S\frac{d\bar{B}}{dS} + \frac{S^2}{2}\frac{d^2\bar{B}}{dS^2} - \delta_m\right] \times \frac{S(1 + D_B)}{[(1 + D_B)S - S_m]^{3/2}} e^{-\frac{(\bar{B}(S)-\delta_m)^2}{2(1+D_B)S-2S_m}}. \quad (32)$$

In order to test the robustness of our expression we ran a series of Monte Carlo random walks[51] and solved the exact multiplicity function for various conditions (δ_m, S_m). In particular we show in Fig. 5 the case where

$D_B = 0.4$ and $\bar{B} = 1.673 + \beta S^\gamma$ with $\gamma = 0.5$ in the upper panel and $\gamma = 3/2$ in the lower panel, both with $\beta = 0.1$. For every test we performed (including the case where δ_c is given by Eq.(12)), a good agreement between the exact solution and Eq.(32) has been achieved.

In the case where $\bar{B} = \delta_c + \beta S^\gamma$, with $\gamma \leq 1$, the second derivative in Eq.(20) can be omitted. This is the case for the modified gravity model we consider here, in the limit of small perturbation $\delta_m \to 0$.

From Eqs.(32,21) we obtain the following linear halo bias in Eulerian space:

$$b_h(S) = 1 + \left\{ \frac{\bar{B}}{S(1 + D_B)} - \frac{1}{\bar{B} - S\frac{d\bar{B}}{dS}} \right\}, \quad (33)$$

This expression is valid for a drifting diffusive barrier defined by Eq.(27) and in particular for $\bar{B} = \delta_c(S) + \beta S$, with δ_c defined by Eq.(12). The parameters β and D_B are fixed by the halo mass function.

V. $f(R)$ **HALO PROFILES**

The structure of dark matter halos is well-known in GR (e.g. [70][71][72]). Their profiles are in good agreement with the NFW fit [71], given by

$$\rho(r) = \frac{\rho_s}{(r/r_s)(1 + r/r_s)^2}, \quad (34)$$

where ρ_s paramterizes the amplitude of the density profile and the scale radius r_s characterizes where the logarithmic slope of the density profile changes.

In Fig. 6, we compare the halo density profiles in our $f(R)$ simulations to the profiles obtained for GR. Results are shown for halos of different mass and at different redshifts. The radii are given in units of $r_{200\text{crit}}$, the spherical overdensity radius within which the average density is 200 times the critical density of the Universe. The mass enclosed in this radius is called $M_{200\text{crit}}$. Overall the differences at fixed $M_{200\text{crit}}$ are rather minor, except maybe for the very central region. For $r > r_{200\text{crit}}$ the deviations in the density profile between $f(R)$ and GR are typically $< 10\%$ for all considered values of f_{R0}. Near the centre, for $r \lesssim r_{200\text{crit}}$ deviations can be larger and reach in some cases a density increase of up to $\sim 40\%$ compared to GR. The f_{R0} value for which the largest deviations are observed seem to depend on halo mass and redshift. This is consistent with the findings of [77]. The observed trend suggests that the largest deviations in the profile shape from GR are observed for objects near the screened/unscreened transition as has also been found for the velocity dispersion profiles [78].

In order to use the profiles in a halo model for the matter power spectrum, we need to be able to convert the halo mass to the profile parameters ρ_s and r_s. As the effects of $f(R)$ on the profiles at fixed mass are largely confined to the very central region which only contribute very little to the matter power spectrum at the wavenumbers we consider here [79], we choose to use the same mass-dependent NFW fits for both GR and $f(R)$. The $f(R)$ effect on the matter power spectrum is then given by the difference in the halo mass function.

A very useful quantity for computing the profile parameters is the halo concentration, which can be defined by $c_{200\text{crit}} \equiv r_{200\text{crit}}/r_s$. In the following we use the model for halo concentration as a function of halo mass from [80], which is a modified version of the model presented in [81]. Predictions of this model are shown to compare well to LCDM simulations of cosmic structure formation in different cosmologies and at different redshifts [82]. The main steps in this model for obtaining the concentration from $M_{200\text{crit}}$ are

- Defining a characteristic mass M_*, whose assembly redshift relates to the concentration. Here a constant fraction of the viral mass, $M_* = F \times M_{200\text{crit}}$, is assumed. In the following we use $F = 0.01$ in agreement with [80].

- Based on the spherical collapse model a collapse, redshift z_c is found which satisfies $\sigma(z_c, R(M_*)) = \delta_c$. As the concentration is not particularly sensitive to the exact value of the collapse threshold, we here assume $\delta_c = 1.686$ for simplicity.

- The concentration is then obtained by $c_{200\text{crit}}(z) = K_{200\text{crit}} \times (\frac{\rho_{\text{crit}}(z_c)}{\rho_{\text{crit}}(z)})^{1/3}$.

As illustrated in Fig. 6, we obtain good agreement with the density profiles in our simulations for $K_{200\text{crit}} = 3.4$. The same value was found to fit a simulation based on a WMAP3 cosmology well in [80].

Once $c_{200\text{crit}}$ is known for a given $M_{200\text{crit}}$, the corresponding ρ_s and r_s can then be obtained by considering

$$M_{200\text{crit}} = \int_0^{r_{200\text{crit}}} dr \, 4\pi r^2 \rho(r) = 4\pi \frac{\rho_s r_s^3}{g(c_{200\text{crit}})}, \quad (35)$$

where

$$g(c) \equiv \frac{1}{\ln(1 + c) - c/(1 + c)}. \quad (36)$$

Using $M_{200\text{crit}} = 200\rho_{\text{crit}}(z)\frac{4}{3}\pi r_{200\text{crit}}^3$, we find

$$\rho_s = 200\rho_{\text{crit}}(z)\frac{g(c_{200\text{crit}})c_{200\text{crit}}^3}{3}, \quad (37)$$

while the scale radius is simply given by

$$r_s = \frac{r_{200\text{crit}}}{c_{200\text{crit}}}. \quad (38)$$

This then completely defines the NFW density profile.

The halo concentration model presented above is based on the spherical over density mass $M_{200\text{crit}}$ rather than
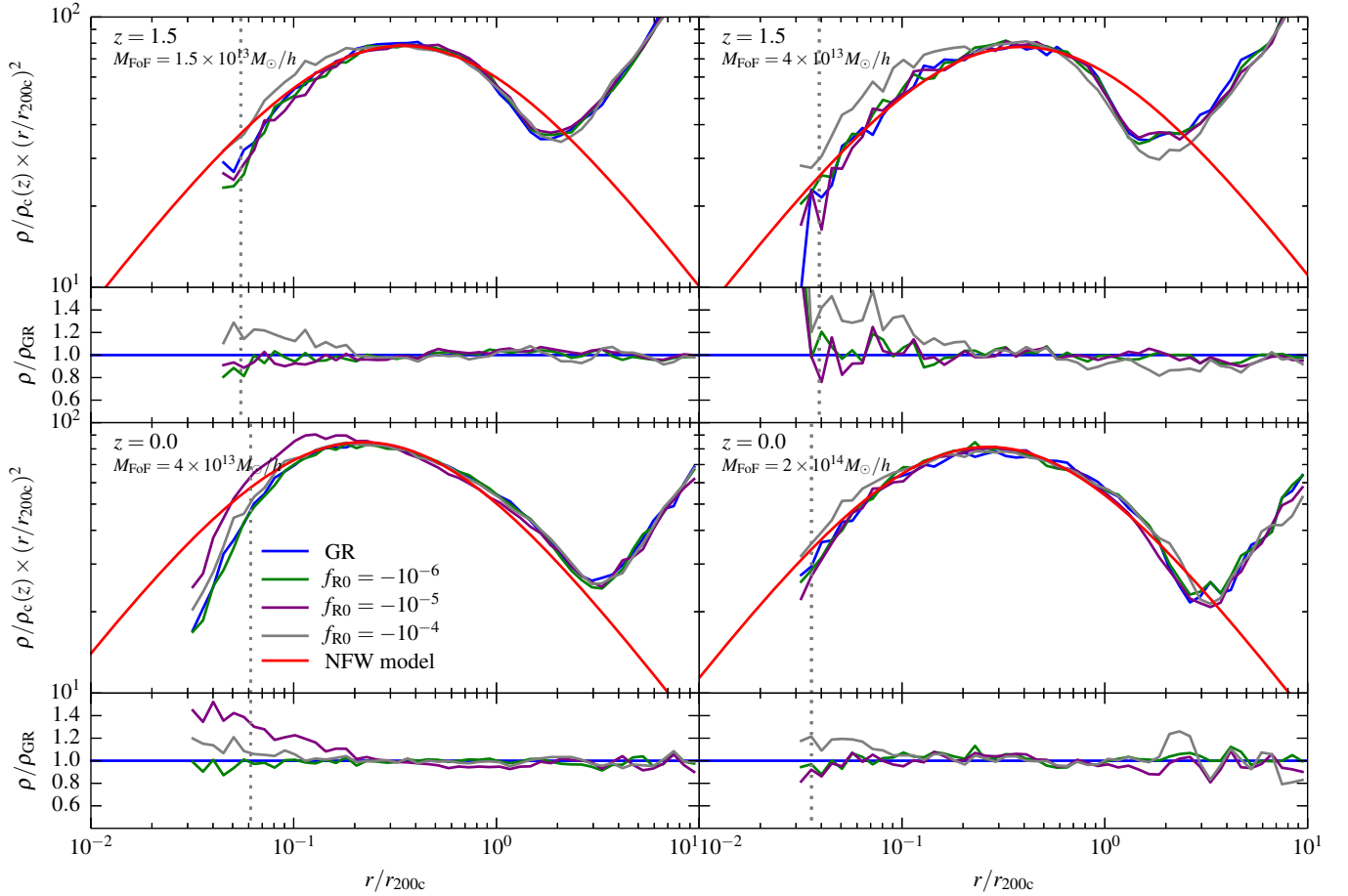
FIG. 6: Density profiles of halos in simulations with GR and $f(R)$. We also compare to the NFW profile obtained from the halo concentration model. The profiles in the larger panels are given in units of the critical density at the considered redshift and have been multiplied by $(r/r_{200c})^2$ to reduce the dependence on radius and allow a more accurate comparison. When plotted in this way the maximum of a NFW profile is attained at the scale radius. The relative differences of the $f(R)$ simulations compared to the GR simulation are shown in the smaller panels. All radii are shown in units of r_{200c}. Results are plotted for $z = 1.5$ (upper panels) and $z = 0$ (lower panels), as well as for different halo mass bins. For the simulations, the mean profiles of all halos with a FoF mass within 20 % of the value indicated in each panel are shown. The NFW profiles have been computed for the quoted FoF mass values. Vertical dotted lines show the gravitational softening in the simulations.

the FoF mass that we have used in section III. To convert between these different mass definitions, we need to make use of the boundary density of FoF groups, which for a linking length of $b = 0.2$ is given by $\Delta_b \approx 82$ times the mean matter density [83]. Assuming spherical symmetry we then obtain the boundary radius, r_{FoF} of the FoF group from $\rho(r_{\text{FoF}}) = \Delta_b \times \rho_{\text{mean}}(z)$. Inserting Eqn. (34) and solving for r_{FoF} we find

$$r_{\text{FoF}} = \frac{r_s}{3}(-2 + x + \frac{1}{x}), \tag{39}$$

where

$$x = \frac{2^{1/3}}{(2 + 27y + 3\sqrt{12y + 81y^2})^{1/3}}, \tag{40}$$

and

$$y = \frac{\rho_s}{\Delta_b \rho_{\text{mean}}(z)}. \tag{41}$$

In analogy to Eq. (35), the FoF mass can then be computed by

$$M_{\text{FoF}} = 4\pi \frac{\rho_s r_s^3}{g(\frac{r_{\text{FoF}}}{r_s})}. \tag{42}$$

In practice, we proceed in the following way to obtain the profile of a halo with a given FoF mass. We start with a grid of $M_{200\text{crit}}$ values that spans the relevant range. For each value, we then compute $c_{200\text{crit}}$, ρ_s, r_s and M_{FoF} as detailed above. In the list that we obtain in this way, we can then interpolate in M_{FoF} to get the NFW parameters ρ_s and r_s for any given FoF mass.
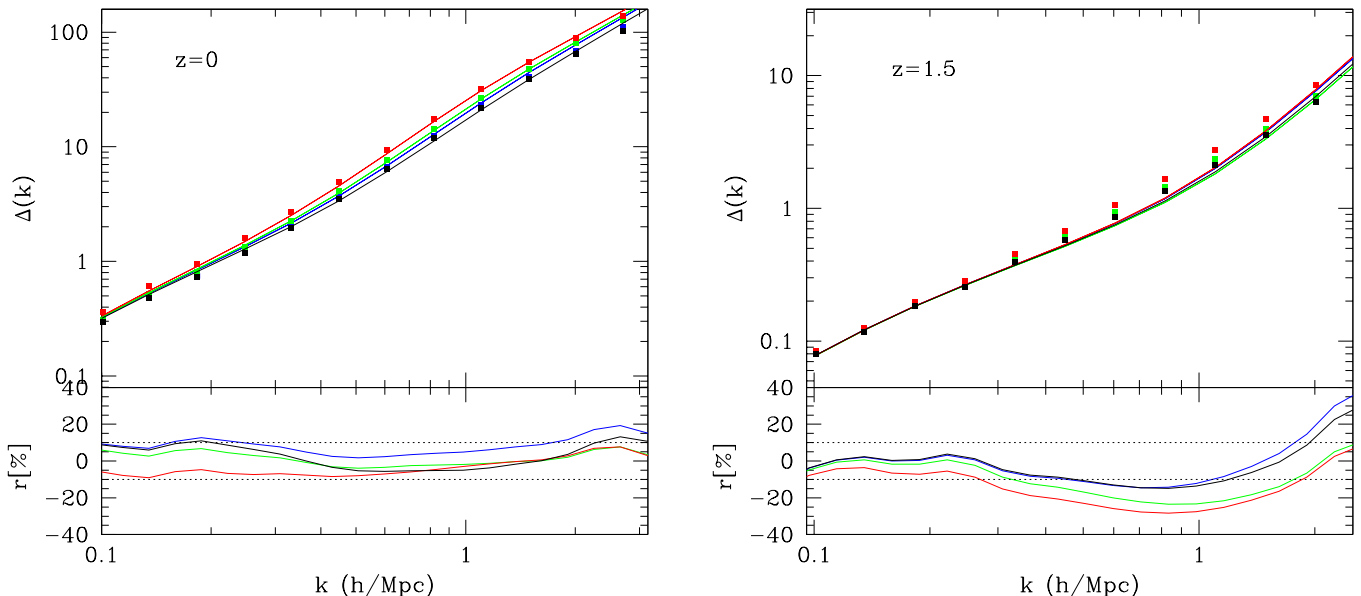
FIG. 7: In the upper panel is the measured non-linear power spectrum at $z = 0$ for GR (black), $f_{R0} = -10^{-6}$ (blue), $f_{R0} = -10^{-5}$ (green) and $f_{R0} = -10^{-4}$ (red) plotted in squares and the halo model prediction (solid lines). Lower panel: relative difference between the measured and predicted $\Delta(k)$ at $z = 0$ (upper panel) and $z = 1.5$ (lower panel).

VI. HALO MODEL: NON-LINEAR MATTER POWER SPECTRUM

In this section we use the halo model [84] to compute the non-linear power spectrum for the modified gravity $f(R)$ model. We test our prediction with N-body simulations. In the halo model, the non-linear power spectrum is given by

$$P(k) = P^{1h}(k) + P^{2h}(k), \tag{43}$$

where P^{1h}, P^{2h} are the one- and two-halo terms:

$$P^{1h}(k) = \int dm \frac{d\,n(m)}{dM} \left(\frac{m}{\bar{\rho}} \right)^2 |u(k|m)|^2, \tag{44}$$

$$P^{2h}(k) \simeq \left[\int dm \frac{d\,n(m)}{dM} \left(\frac{m}{\bar{\rho}} \right) u(k|m)b(m) \right]^2 P^{lin}(k). \tag{45}$$

The $u(k|m)$ is the Fourier transform of the dark matter distribution within a halo of mass m, (see Eq.80 in [84]), dn(M)/dM is the halo mass function, $b(M)$ is the linear halo bias and $P^{lin}(k)$ the linear dark matter power spectrum. These equations assume that at any redshift, all dark matter is contained in halos. This is not exactly the case for the ΛCDM model, especially for non-spherical collapse [56].

In order to predict the non-linear power spectrum, we use the halo mass function in Eq.(8) with the multiplicity function of Eq.(15) calibrated with the parameters $\delta_c(M), \beta, D_B$ given by Eq.(12) and Table I. Those parameters also set the linear Eq.(33). For the profile of halos, we use the GR values of the concentration parameters in the NFW profile that we computed in Sec.V.

In addition, due to the numerical limitation of the integrated mass range, we ensure that the halo term with the largest contribution to the power spectrum equals the linear theory expression on large scale by renormalizing the linear bias with a factor q. Following the procedure of [85][86], we compute q as follow:

$$\int_{m_{min}}^{m_{max}} dm\, m\, \frac{n(m)}{\bar{\rho}} \frac{b(m)}{q} = 1. \tag{46}$$

In Fig. 7 we can see the power spectrum at $z = 0$ obtained from the N-body simulations for $f_{R0} = -10^{-4}, -10^{-5}, -10^{-6}$ and GR shown by the red, green, blue and black squares respectively. The associated solid lines show the halo model predictions. The relative differences between theory and N-body simulations are shown on the lower panel of Fig 7. Our predictions for the halo model lead to $\sim 10\%$ accuracy with respect to N-body simulations at $z = 0$. Similarly to previous studies [89–91], the accuracy of the predictions decreases for higher redshift up to $\sim 35\%$ at $z = 1.5$ for $f_{R0} = -10^{-4}$ and

$\sim 20\%$ for GR. This can be seen in the lower panel of Fig. 7.

Overall we note that the $f(R)$ models increase the power, particularly on small spatial scales $k \gtrsim 0.5h\mathrm{Mpc}^{-1}$. For $k = 1h\mathrm{Mpc}^{-1}$, the relative difference to GR reaches up to $\sim 45\%$ at $z = 0$, ($\sim 30\%$ at z=1.5). Our results are similar to those found in [89, 91, 92]. We note that our predictions could potentially be improved using a halo profile which would reproduce low mass halo profiles more accurately at high redshift, (see recent work [93] in this perspective). However, as we already mention, the halo model assumed all the dark matter to be contained inside halos. This approximation is worse for higher redshift, (e.g. [94]).

VII. VOID ABUNDANCES

Due to the presence of the screening mechanism, cosmic voids can potentially be very powerful tools to constrain $f(R)$ models, as the central parts of the voids are expected to be unscreened due to their low matter density, while the void walls could be fully or partially screened. Hence voids provide the opportunity to test the transition between these two regimes. **In particular, while the abundance of voids can provide a test of the enhanced growth of linear density perturbations due to an unscreened fifth-force, the shape of voids around their boundaries might be less affected due to the nonlinear screening, thereby providing a way to disentagle the effect of the modified gravity theory from other cosmological models characterised by an enhanced perturbation growth (as e.g. clustering or coupled Dark Energy).** Several works have been focusing on measuring the void abundance and its deviation from the expectations of the standard ΛCDM model in the context of various non-standard cosmologies (e.g. [28, 88, 95, 96, 102]). In particular, for the case of $f(R)$ gravity, some of these works [88, 95, 96] have shown that there is an excess of large voids compared to ΛCDM, and that the excess is larger for larger values of the f_{R0} parameter. This confirms the intuitive prediction that the action of the fifth force pushes the particles stronger towards the void wall [97], thereby more efficiently evacuating the void centres. However, most of these analysis are based on cosmic voids identified in some random subsampling of the dark matter density field, while voids are generally identified in galaxy surveys. The effect of the tracer bias and of the CDM particle sampling on analytical predictions for the void abundance is still an unsolved issue for the standard ΛCDM case [see e.g. 27, 28, 98, 100]. Recently, [96] have compared the abundance and the density profiles of voids identified using the halo catalogs of some $f(R)$ simulations to the case where voids are identified in a random subsample of CDM particles, finding that the deviations with respect to the ΛCDM cosmology are much weaker when halos are used
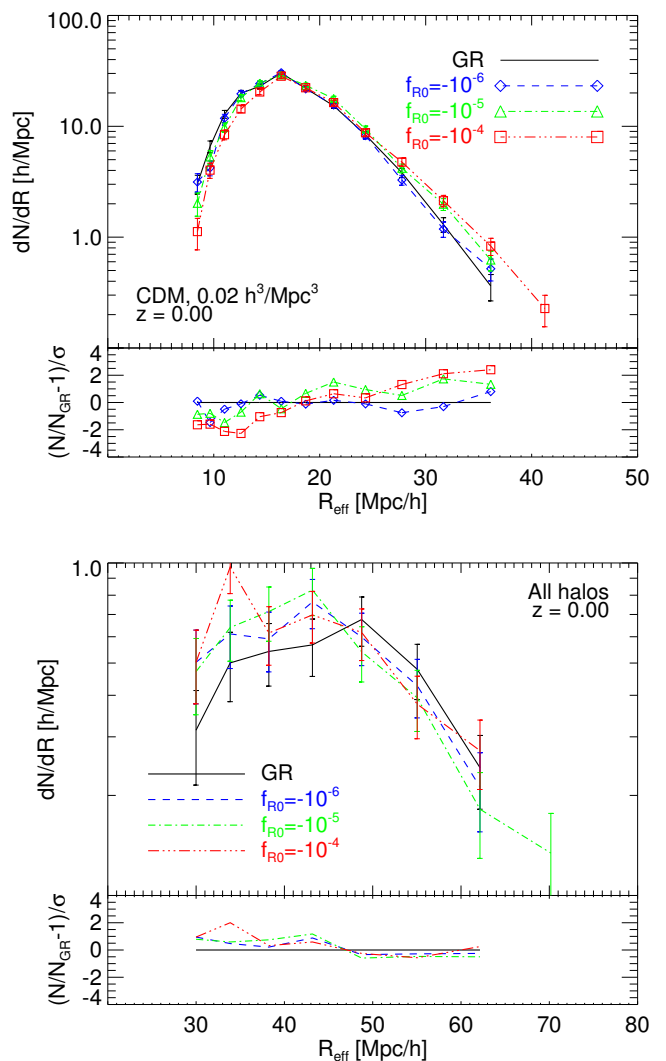

FIG. 8: *Upper panel* – Void abundance detected in the CDM density field using VIDE and a random subsampling of the CDM particles with a density of 0.02 particles per cubic Mpc/h. *Lower Panel* – The same quantity for the sample of voids identified in the FoF halo catalog.

as density tracers. A similar conclusion has been reached by [28] for interacting dark energy models. In this paper, we focus on void abundances and profiles detected in the simulations of [48] using the VIDE void finder [26], based on the ZOBOV code [104]. Nonetheless, we adopt a slight modification [28] of the void hierarchy classification provided by VIDE which allows to eliminate possible pathological voids and to obtain a converging void abundance when changing the sparsity of the density tracers.

Specifically, for each $f(R)$ model and for the standard GR simulations we have run VIDE on both a random subsampling of the CDM particles (with an average density of 0.02 particles per cubic Mpc/h), and on the positions of the FoF halos identified in the simulations (having an average density of about 8.4×10^{-4} halos per cu-

bic Mpc/h), both at $z = 0$. In order to avoid multiple counting of the volume included in sub-voids within a complex void hierarchy we have selected only the main voids, i.e. those voids that are not part of larger voids. Furthermore, among these voids we have defined two selection criteria to remove possible pathological voids (see [28]), namely requiring a minimum void density $\rho_{\rm v,min}$ lower than 0.2 times the average density and a density contrast (i.e. the density ratio between the density minimum $\rho_{\rm v,min}$ and the void boundary $\rho_{\rm v,bound}$) larger than 1.57 (see [104]). If a given main void identified by VIDE does not fulfil both these criteria we remove it from our catalog and we promote all its first tier of sub-voids to the role of main voids. This selection procedure is then repeated until no pathological main voids are left in the sample. This procedure allows to obtain a robust sample of main voids whose abundance does converge (down to the resolution scale allowed by the density of the tracers) for different random sub-samplings of the original CDM density field or different densities of the FoF halo sample.

In Fig. 8 we show the size distribution of cosmic voids identified as a function of their effective radius $R_{\rm eff}$ defined from the void volume V assuming spherical symmetry. The upper panel shows the result obtained for voids identified based on our random sub-sampling of the CDM particle distribution, while the lower panel displays the same quantity obtained from the FoF halo catalogue. In each panel, the upper plot shows the number of voids as a function of their radius, where the error bars represent the Poisson error associated with the number counts in each bin, while the lower plot shows the significance of the relative difference between each $f(R)$ model and standard GR. It is interesting to notice that the two plots show a very different relative trend among the models. While in the halo voids sample we do not observe significant deviations between the different gravity models except for a mild excess of large voids for the ΛCDM and the $f_{R0} = -10^{-6}$ case, in the CDM voids sample the trend is the opposite and presents a much higher significance, with all the $f(R)$ scenarios showing a higher abundance of large voids as compared to ΛCDM. This stark difference in the relative behaviour of the expected size distribution of cosmic voids, when the latter are identified using a biased vs. an unbiased set of tracers of the underlying CDM density field, has been already pointed out by [96] for the case of $f(R)$ gravity, and more recently by [27, 28, 100]. This can be explained as a consequence of the different bias that a population of halos within the same mass range is found to have in different gravity models: while the additional gravitational force acting in $f(R)$ cosmologies is effective in evacuating the voids from the smooth CDM component, thereby increasing the amplitude of CDM density perturbations (and consequently the size and depth of cosmic voids, see the next section), the bias of collapsed objects is substantially reduced in these scenarios with respect to standard gravity, so that the net effect on amplitude and size of perturbations in the halos population is reduced (see[28]). **This inter-**

pretation is consistent with the results obtained by other recent studies on the abundance of cosmic voids in coupled Dark Energy [28] and massive neutrino cosmologies [101]. In both cases, in fact, the abundance of voids in the CDM distribution is significantly affected by an enhanced growth (due to the Dark Energy interaction) for the former and by a suppressed growth (due to neutrino free-streaming) for the latter, while the abundance of voids in the halo/galaxy distribution – having a lower bias and a higher bias in the two cases, respectively – shows much weaker features. More specifically, the effect of halo bias has been explicitly tested in [28] and [27] by comparing the void size distributions obtained in a randomly subsampled CDM distribution having the same density of tracers as the corresponding halo catalog, and finding that the bias significantly affects the voids distribution.

It is interesting to see that this effect is still present for different void finders. In [96] the authors used a spherical shell to identify voids in the distribution of halos **and found that the halo number density profile of $f(R)$ models around the void center is shallower (i.e. closer to the GR case) than the corresponding CDM density profile (see e.g. Figs. 9 and 13 of [96]). However, in the analysis of [96]** the authors had find a ratio of the number of voids in $f(R)$ gravity to GR of $N_{f(R)}/N_{\rm GR} \sim 0.3$ for $R \sim 45 {\rm Mpc}/h$ in the $f_{R0} = -10^{-4}$ case, while we do not measure a lower number of voids on this scale. Therefore using the abundance of voids to discriminate between GR and $f(R)$ gravity must be taken with some caution. Depending on the algorithm used to identify voids, the population of tracers (dark matter Vs. halos), and their number density, different results can be obtained.

VIII. VOID PROFILES

Void profiles have been extensively studied in the recent literature. In particular, several studies (see e.g. [32, 33, 103]) have claimed the self-similarity of the density profiles of cosmic voids in the standard ΛCDM model, which would make the shape of voids an ideal geometrical probe of the underlying cosmology. As mentioned before, in the context of $f(R)$ gravity, recent works (as e.g. [95, 96, 105]) have shown that the extra force has the effect of evacuating faster the inner regions of cosmic voids, thereby producing steeper void profiles. A similar result is found for interacting dark energy models, even in the absence of a scale-dependent screening mechanism ([28, 102]). Here we compute the void density profiles in our set of $f(R)$ simulations using two different approaches:

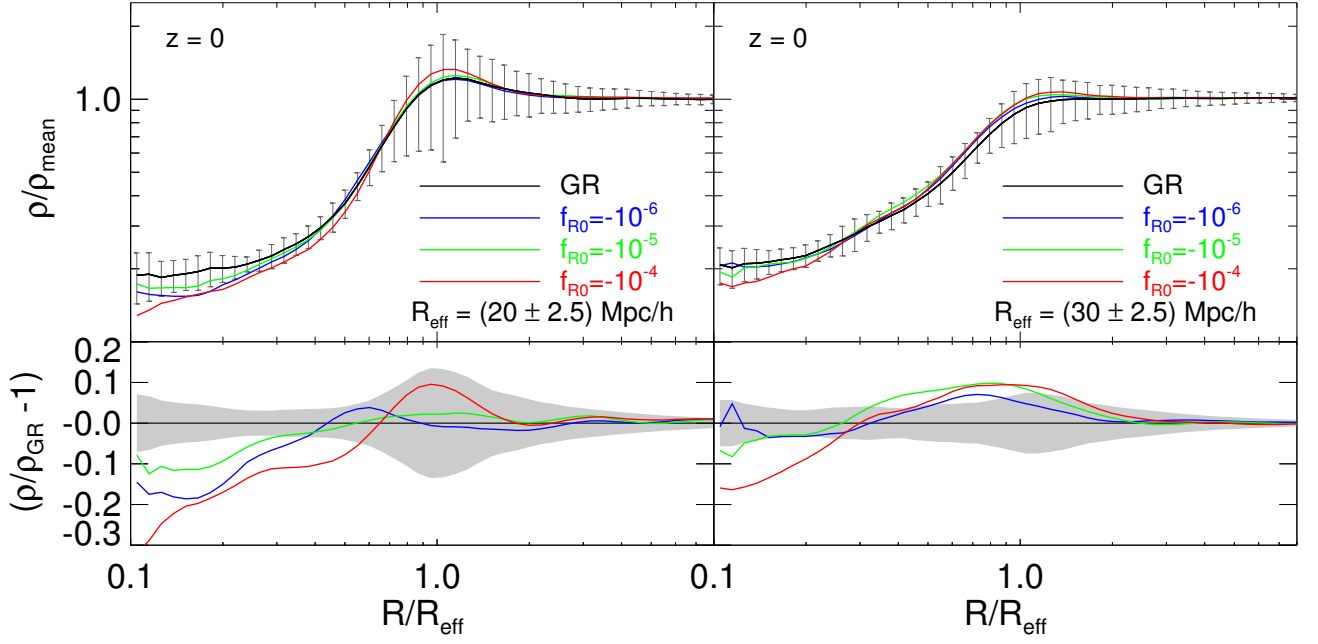(i) stacking density profiles using void centres of each simulation

FIG. 9: Stacked density profiles using the void centres of each simulation.
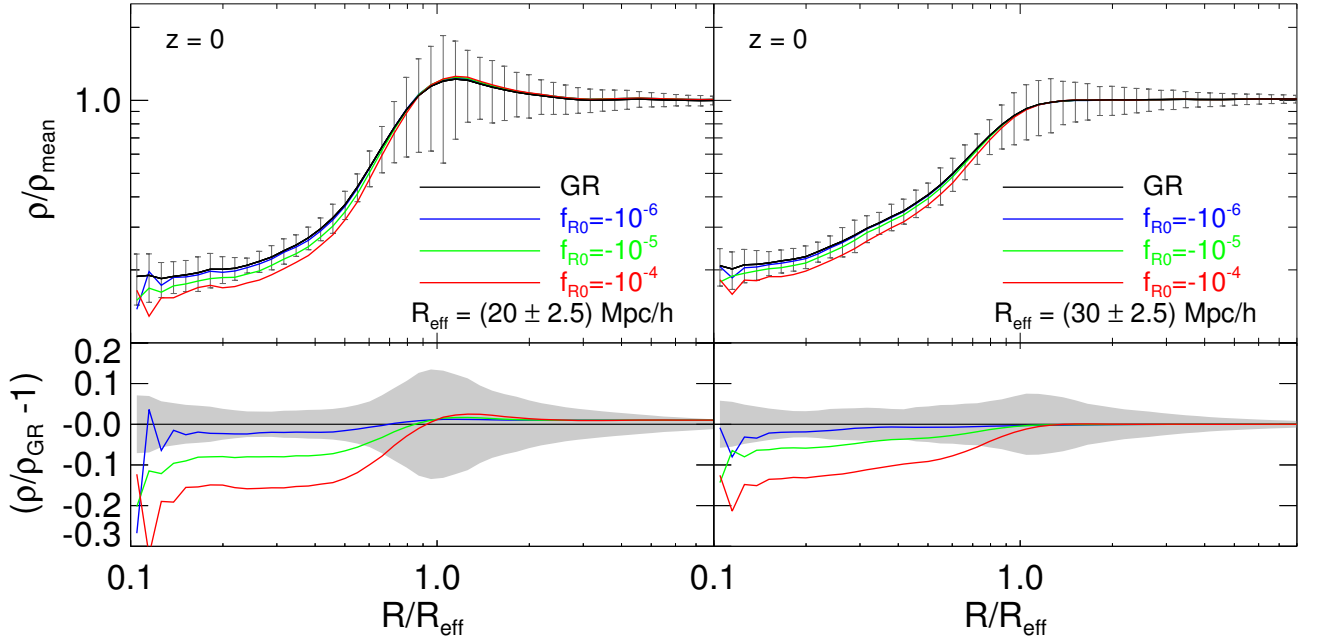

FIG. 10: Stacked density profiles using the void centres of the GR simulation.

(ii) stacking density profiles using the centres of the GR simulation.

The latter approach allows us to to test more precisely the effect of $f(R)$ since all simulations start from the same initial conditions. Therefore, by doing this one-to-

one comparison, we avoid fluctuations in the profiles due to the selection of voids using VIDE. Any deviations from the GR profiles are due to the $f(R)$ gravity.

To this end, we first compute the spherically-averaged radial density profile of each individual void by estimating the CDM density within a series of logarithmically equispaced spherical shells centred in the barycentre of

each void and normalised to the void effective radius R_{eff}. We perform this procedure for two distinct ranges of void size, namely $R_{\text{eff}} = \{20, 30\} \pm 2.5$ Mpc/h, considering 100 randomly selected voids in each case. Then we obtain the stacked profiles by averaging the overdensity in each radial bin over the 100 individual profiles. The resulting profiles are displayed in Fig. 9, where we show the comparison of the stacked density profiles obtained using the CDM void catalog in standard GR and in the various realisations of $f(R)$ gravity. In the upper panels of Fig. 9 the error bars represent the corrected sample standard deviation computed on the 100 randomly selected voids, while in the lower panels we show the relative difference between the models and the grey-shaded area represents the 2σ confidence on the relative difference based on the standard deviation of the mean density profiles computed through a *bootstrap* resampling technique with 1000 re-samples of the 100 individual profiles. As the figure shows, $f(R)$ voids present a systematically lower density in the inner part of the void with a significant deviation from the GR behavior.

In Fig. 10 we show the same results obtained by computing the individual spherically-averaged profiles, always assuming, i.e. for all gravity models, the void centre computed from the GR simulation. This results in a clearer hierarchy among the models in the overdensity deviation from GR that appears in the central part of the voids, with the deviation increasing for increasing values of the f_{R0} parameter. As one can see from the figure, only the $f_{R0} = -10^{-6}$ model is found to be consistent at 2σ with the GR result, while the other models are both clearly distinguishable from the standard case.

To conclude this section, the imprint of $f(R)$ in the void profiles is enhanced near the centres of voids and for smaller void sizes with significant deviations from the GR case except for the weakest modification of gravity considered in the present work.

IX. CONCLUSIONS

(i) In this paper we performed an analysis of the $f(R)$ imprints on the large scale structure of the Universe in the non-linear domain. We started by looking at the halo abundance measured in N-body simulations. We used the theoretical model of [44] to fit the multiplicity function and found a good accuracy with the N-body simulations up to $z = 1.5$. Overall we found a larger number of massive halos in $f(R)$ gravity, which agrees with previous studies (e.g. [68][96]. However, unlike previous studies (e.g. [68]) we found the drifting diffusive barrier mass function reproduces the $f(R)$ N-body simulations also in the low halo masses regime.

(ii) We extended the theoretical multiplicity function to the conditional one. We used Monte Carlo random walks to ensure the robustness of our prediction and we found a very good correspondence for different large scale perturbations at the $\sim 5\%$ level. From this prediction we

derived the linear halo bias for $f(R)$ gravity. The latter is fixed by the parameters of the halo mass function and in particular the linear criteria of collapse, (stochastic barrier). Because most of the stochastic nature of the barrier is due to the excursion set framework [61][62], our prediction of the conditional mass function can be easily extended to any theory of gravity, providing the linear spherical criteria for halos to collapse.

(iii) We measured the halo density profiles in the $f(R)$ and GR N-body simulations. We found a deviations from GR depending on the halo masses, redshift and f_{R0} parameters. This deviation tends to decrease for massive halos at low redshift (e.g. $2 \times 10^{14} M_{\odot}/h$ at $z = 0$). However, it is unclear how to model the trend of these profiles considering that the amount of the deviations are not necessarily proportional to the modified gravity parameter f_{R0}. In [106], the author study how the NFW profile varies with cosmology and quantify this information in an observable quantity named sparicity. It would be interesting to see if this quantity can be used to probe the $f(R)$ gravity.

(iv) Neglecting the difference between GR and $f(R)$ halo profiles at fixed halo mass, we used the halo model with our predictions of the linear halo bias and halo mass function to predict non-linear clustering. For the GR case we found an agreement on the order of $\sim 10\%$ at $z = 0$ and 20% at $z = 1.5$ for $k \leqslant 2h\text{Mpc}^{-1}$. On the other hand for the $f_{R0} = -10^{-4}$ case the agreement between our prediction and the N-body measurement is $\sim 10\%$ at $z = 0$ and only $\sim 35\%$ at $z = 1.5$. Overall we provide a simple prediction of the non-linear power spectrum which qualitative agree with the $f(R)$ simulation at $z = 0$.

(v) We studied the void number density detected in $f(R)$ and GR simulations. We tested the effect of the bias and sampling by considering as tracers both dark matter particles and halos. We found more voids in the dark matter density field in the case of $f(R)$ gravity. This was already observed in previous studies and with different void finders (e.g.[96]). However, this effect is erased when we identified voids using halos. In this case the ratio between $f(R)$ voids to GR depends on the number density and the void finder.

(vi) We tested the imprint of $f(R)$ on the void density profiles using a standard stacking technique and a one-to-one comparison between the GR profiles and the $f(R)$ cases. In all case we found that void densities are lower in $f(R)$ compared to GR. This qualitatively agree with [96][95][105].

[1] Ahn C. P., Alexandroff R., Allende Prieto C., et al., 2013, arXiv:1307.7735
[2] Hill G. J., et al., 2008, ASP Conf. Ser., 399, 115
[3] Ivezic Z., et al., 2008, arXiv:0805.2366
[4] Abbott T., et al., 2005, arXiv:astro-ph/0510346
[5] Michael Levi et al., arxiv: 1308.0847
[6] http://www.sdss.org/surveys/eboss/
[7] http://wfirst.gsfc.nasa.gov/
[8] Kaiser N., et al., 2002, Proc. SPIE Int. Soc. Opt. Eng., 4836, 154
[9] Laureijs R., Amiaux J., Arduini S., et al., 2011, arXiv:1110.3193
[10] Riess et al., The Astronomical Journal, Volume 116, Issue 3, pp. 1009-1038
[11] Perlmutter et al., The Astrophysical Journal, Volume 517, Issue 2, pp. 565-586
[12] C. Blake et al., Monthly Notices of the Royal Astronomical Society, Volume 418, Issue 3, pp. 1707-1724.
[13] Planck 2013 results. XVI. Cosmological parameters, Astronomy & Astrophysics, Volume 571, id.A16, 66 pp.
[14] Wetterich, C., Nuclear Physics B, Volume 302, Issue 4, p. 645-667.
[15] Raphael Bousso, arxiv: 1203.0307
[16] Peebles, P. J. E.; Ratra, Bharat, Astrophysical Journal, Part 2 - Letters to the Editor (ISSN 0004-637X), vol. 325, Feb. 15, 1988, p. L17-L20
[17] Farrar, Glennys R.; Peebles, P. J. E., The Astrophysical Journal, Volume 604, Issue 1, pp. 1-11.
[18] C. Wetterich, Astronomy and Astrophysics, v.301, p.321
[19] L. Amendola, Physical Review D (Particles, Fields, Gravitation, and Cosmology), Volume 62, Issue 4, 15 August 2000, id.043511
[20] Amendola, Luca; Baldi, Marco; Wetterich, Christof, Physical Review D, vol. 78, Issue 2, id. 023015
[21] Khoury, Justin; Weltman, Amanda, Physical Review D, vol. 69, Issue 4, id. 044026
[22] Matteo Cataneo et al., Phys. Rev. D 92, 044009 (2015)
[23] Eduardo Rozo et al., arxiv: 0703.571
[24] Mana et al., Monthly Notices of the Royal Astronomical Society, Volume 434, Issue 1, p.684-695 (2013)
[25] Baldi, Marco, Monthly Notices of the Royal Astronomical Society, Volume 411, Issue 2, pp. 1077-1103 (2011)
[26] Sutter, P. M.; Lavaux, G.; Hamaus, N.; Pisani, A.; Wandelt, B. D.; Warren, M.; Villaescusa-Navarro, F.; Zivick, P.; Mao, Q.; Thompson, B. B., Astronomy and Computing, Volume 9, p. 1-9, (2015)
[27] Nadathur, Seshadri; Hotchkiss, Shaun, eprint arXiv:1507.00197
[28] G. Pollina, M. Baldi, F. Marulli and L. Moscardini, eprint arXiv:1506.08831.
[29] Starobinsky A. A., Physics Letters B, Volume 91, Issue 1, p. 99-102.
[30] Hu, Wayne; Sawicki, Ignacy, Physical Review D, vol. 76, Issue 6, id. 064004
[31] H.A. Buchdahl, Monthly Notices of the Royal Astronomical Society, Vol. 150, p. 1 (1970)
[32] Ricciardelli, E.; Quilis, V.; Planelles, S., Monthly Notices of the Royal Astronomical Society, Volume 434, Issue 2, p.1192-1204
[33] Ricciardelli, E.; Quilis, V.; Varela, J., Monthly Notices of the Royal Astronomical Society, Volume 440, Issue 1, p.601-609 (2014)
[34] Oyaizu, H. 2008, Phys. Rev. D , 78, 123523
[35] Oyaizu, Hiroaki; Lima, Marcos; Hu, Wayne, Physical Review D, vol. 78, Issue 12, id. 123524
[36] Li, Baojiu; Zhao, Gong-Bo; Teyssier, Romain; Koyama, Kazuya, Journal of Cosmology and Astroparticle Physics, Issue 01, id. 051 (2012)
[37] Llinares, Claudio; Mota, David F., Physical Review Letters, vol. 110, Issue 16, id. 161101
[38] Bertotti, B.; Farinella, P.; Vokrouhlick, D., ADS bibliographic: 2003ASSL..293.....B
[39] Clifford M. Will, Living Reviews in Relativity, vol. 9, no. 3
[40] Sotiriou & Faraoni, Reviews of Modern Physics, vol. 82, Issue 1, pp. 451-497
[41] Dvali, G.; Gabadadze, G.; Porrati, M., Physics Letters B, Volume 485, Issue 1-3, p. 208-214.
[42] Pogosian & Silvestri, Physical Review D, vol. 77, Issue 2, id. 023503
[43] Nicolis, Alberto; Rattazzi, Riccardo; Trincherini, Enrico, Physical Review D, vol. 79, Issue 6, id. 064036
[44] Kopp, Michael; Appleby, Stephen A.; Achitouv, Ixandra; Weller, Jochen, Physical Review D, vol. 88, Issue 8, id. 084015
[45] Lombriser, L. 2014, Annalen der Physik, 526, 259
[46] Terukina, A., Lombriser, L., Yamamoto, K., et al. 2014, Journal of Cosmology and Astroparticle Physics, 4, 013
[47] Jain, B., Vikram, V., & Sakstein, J. 2013, Astrophys. J. , 779, 39
[48] Puchwein, Ewald; Baldi, Marco; Springel, Volker, Monthly Notices of the Royal Astronomical Society, Volume 436, Issue 1, p.348-360
[49] Noller, J., von Braun-Bates, F., & Ferreira, P. G. 2014, Phys. Rev. D , 89, 023521
[50] Arnold, C., Puchwein, E., & Springel, V. 2014, Mont., Not. Roy. Astron. Soc., 440, 833
[51] J. R. Bond, S. Cole, G. Efstathiou & G. Kaiser, Astrophys. J. **379**, 440 (1991)
[52] W. H. Press & P. Schechter, Astrophys. J. **187**, 425 (1974)
[53] M. Maggiore & A. Riotto, Astrophys. J. **711**, 907 (2010)
[54] M. Maggiore & A. Riotto, Astrophys. J. **717**, 515 (2010)
[55] P.S. Corasaniti and I.E. Achitouv,Phys. Rev. Lett. **106**, 241302 (2011)
[56] P.S. Corasaniti and I.E. Achitouv, Phys. Rev. D **84**,

023009 (2011)

[57] I. Achitouv & P.S Corasaniti, JCAP 02 (2012) 002

[58] E. Audit, R. Teyssier & J.-M. Alimi, Astron. & Astrophys. **325**, 439 (1997)

[59] R.K. Sheth, H. J. Mo & G. Tormen,Mont. Not. Roy. Astron. Soc. **323**, 1 (2001)

[60] Vikhlinin, A. A.; Kravtsov, A. V.; Markevich, M. L.; Sunyaev, R. A.; Churazov, E. M., Physics Uspekhi, Volume 57, Issue 4, article id. 317-341 (2014).

[61] Achitouv, I.; Rasera, Y.; Sheth, R. K.; Corasaniti, P. S., Physical Review Letters, vol. 111, Issue 23, id. 231303

[62] Achitouv, I.; Wagner, C.; Weller, J.; Rasera, Y., JCAP10(2014)077

[63] J. M. Bardeen, J. R. Bond, N. Kaiser A. Szalay, Astrophys. J. 304, 15 (1986).

[64] S. Cole, N. Kaiser, Mont. Not. Roy. Astron. Soc. 237,1127 (1989).

[65] H. Mo, S. White, Mont. Not. Astron. Soc. 282, 347(1996).

[66] R. K. Sheth, G. Tormen, Mont. Not. Roy. Astron. Soc.308, 119 (1999).

[67] R. K. Sheth, H. J. Mo, and G. Tormen, Monthly Notices of the RAS, 323, 1 (2001),

[68] Lombriser, Lucas; Li, Baojiu; Koyama, Kazuya; Zhao, Gong-Bo, Physical Review D, vol. 87, Issue 12, id. 123511

[69] C.-P. Ma, M. Maggiore, A. Riotto & J. Zhang, Mont., Not. Roy. Astron. Soc. 411, 2644 (2011).

[70] Cole, Shaun; Lacey, Cedric, M.N.R.A.S., vol. 281, p. 716 (1996)

[71] Navarro, J. F.; Hayashi, E.; Power, C.; Jenkins, A. R.; Frenk, C. S.; White, S. D. M.; Springel, V.; Stadel, J.; Quinn, T. R., Monthly Notices of the Royal Astronomical Society, Volume 349, Issue 3, pp. 1039-1051

[72] Prada, Francisco; Klypin, Anatoly A.; Cuesta, Antonio J.; Betancort-Rijo, Juan E.; Primack, Joel, Monthly Notices of the Royal Astronomical Society, Volume 423, Issue 4, pp. 3018-3030

[73] White, S. D. M.; Rees, M. J., Monthly Notices of the Royal Astronomical Society, vol. 183, May 1978, p. 341-358.

[74] Velliscig, Marco; van Daalen, Marcel P.; Schaye, Joop; McCarthy, Ian G.; Cacciato, Marcello; Le Brun, Amandine M. C.; Vecchia, Claudio Dalla, Monthly Notices of the Royal Astronomical Society, Volume 442, Issue 3, p.2641-2658

[75] Ewa L. Lokas and Gary A. Mamon, Mon. Not. R. Astron. Soc. 321, 155-166 (2001)

[76] Takada, M., & Jain, B. 2003, MNRAS, 340, 580

[77] Hammami, A., Llinares, C., Mota, D. F., Winther, H. A. 2015, MNRAS, 449, 3635

[78] Gronke, M., Llinares, C., Mota, D. F., Winther, H. A. 2015, MNRAS, 449, 2837

[79] van Daalen, M. P., & Schaye, J. 2015, arXiv:1501.05950

[80] Macciò, A. V., Dutton, A. A., & van den Bosch, F. C. 2008, MNRAS, 391, 1940

[81] Bullock, J. S., Kolatt, T. S., Sigad, Y., et al. 2001, MNRAS, 321, 559

[82] Dutton, A. A., & Macciò, A. V. 2014, MNRAS, 441, 3359

[83] More, S., Kravtsov, A. V., Dalal, N., & Gottlöber, S. 2011, ApJS, 195, 4

[84] Cooray, Asantha; Sheth, Ravi, Physics Reports, Volume 372, Issue 1, p. 1-129.

[85] Scoccimarro, R., Sheth, R. K., Hui, L., & Jain, B. 2001, ApJ, 546, 20

[86] Pielorz, J.; Rodiger, J.; Tereno, I.; Schneider, P., Astronomy and Astrophysics, Volume 514, id.A79, 19 pp.

[87] Zhao, Gong-Bo, The Astrophysical Journal Supplement, Volume 211, Issue 2, article id. 23, 12 pp. (2014)

[88] Li, Baojiu; Zhao, Gong-Bo; Koyama, Kazuya, Monthly Notices of the Royal Astronomical Society, Volume 421, Issue 4, pp. 3481-3487.

[89] Lombriser, Lucas; Koyama, Kazuya; Li, Baojiu, Journal of Cosmology and Astroparticle Physics, Issue 03, article id. 021, pp. (2014)

[90] P. Brax and P. Valageas, Phys. Rev. D, 88, 023527 (2013)

[91] G.-B. Zhao, ApJS, 211, 23 (2014)

[92] Li, Baojiu; Hellwing, Wojciech A.; Koyama, Kazuya; Zhao, Gong-Bo; Jennings, Elise; Baugh, Carlton M.,

[93] Mohammed, Irshad; Seljak, Uros, Monthly Notices of the Royal Astronomical Society, Volume 445, Issue 4, p.3382-3400 (2014)

[94] Andrei Lazanu, Tommaso Giannantonio, Marcel Schmittfull, E.P.S. Shellard, arXiv:1510.04075

[95] Zivick, Paul; Sutter, P. M., arXiv1410.0133Z

[96] Cai, Yan-Chuan; Padilla, Nelson; Li, Baojiu, eprint arXiv:1410.1510

[97] Clampitt, Joseph; Cai, Yan-Chuan; Li, Baojiu, Monthly Notices of the Royal Astronomical Society, Volume 431, Issue 1, p.749-766

[98] Jennings, Elise; Li, Yin; Hu, Wayne, Monthly Notices of the Royal Astronomical Society, Volume 434, Issue 3, p.2167-2181

[99] Sheth R. K., van de Weygaert R., 2004, MNRAS, 350, 517

[100] Achitouv, Ixandra; Neyrinck, Mark; Paranjape, Aseem, Monthly Notices of the Royal Astronomical Society, Volume 451, Issue 4, p.3964-3974, Monthly Notices of the Royal Astronomical Society, Volume 428, Issue 1, p.743-755

[101] E. Massara, F. Villaescusa-Navarro, M. Viel and P. M. Sutter, JCAP **1511** (2015) 11, 018

[102] Sutter, P. M. et al., Astronomy and Computing, Volume 9, p. 1-9. (2015)

[103] Hamaus, Nico; Sutter, P. M.; Wandelt, Benjamin D., Physical Review Letters, Volume 112, Issue 25, id.251302

[104] Neyrinck, Mark C., Monthly Notices of the Royal Astronomical Society, Volume 386, Issue 4, pp. 2101-2109

[105] Zivick, Paul; Sutter, P. M.; Wandelt, Benjamin D.; Li, Baojiu; Lam, Tsz Yan, Monthly Notices of the Royal Astronomical Society, Volume 451, Issue 4, p.4215-4222 (2015)

[106] Balmes, I.; Rasera, Y.; Corasaniti, P.-S.; Alimi, J.-M., Monthly Notices of the Royal Astronomical Society, Volume 437, Issue 3, p.2328-2339 (2014)